Unraveling the impact of different thermal quenching routes on the luminescence efficiency of the Y3Al5O12:Ce3+ phosphor for white light

Citation for the original published paper (version of record):
Lin, Y., Bettinelli, M., Sharma, S. et al (2020). Unraveling the impact of different thermal quenching routes on the luminescence efficiency of
the Y3Al5O12:Ce3+ phosphor for white light emitting diodes. Journal of Materials Chemistry C, 8(40): 14015-14027. http://dx.doi.org/10.1039/d0tc03821k

(article starts on next page)

Journal of
Materials Chemistry C

PAPER

Cite this: J. Mater. Chem. C, 2020, 8, 14015

Unraveling the impact of different thermal quenching routes on the luminescence efficiency of the $Y_3Al_5O_{12}:Ce^{3+}$ phosphor for white light emitting diodes†

Yuan-Chih Lin, [a] Marco Bettinelli, [b] Suchinder K. Sharma, [a] Britta Redlich,[c] Adolfo Speghini [d] and Maths Karlsson *[a]

Cerium doped yttrium aluminium garnet, $Y_{3-z}Ce_zAl_5O_{12}$, is the prototype material for solid-state white lighting and it still is an important white LED phosphor. However, fundamental understanding of the thermal quenching of luminescence, which leads to a pronounced reduction of the emission intensity under high-power light-emitting diode operation, remains to be obtained. Here we show, through a multitechnique approach based on photoluminescence, thermoluminescence and mode-selective vibrational excitation experiments that thermal quenching of luminescence in $Y_{3-z}Ce_zAl_5O_{12}$ is caused by a combined effect of thermal ionization, thermally activated concentration quenching, and thermally activated 5d → 4f crossover relaxation *via* electron–phonon coupling, and establish the general trends upon variation of the Ce^{3+} concentration and temperature. Thermal quenching below 600 K is primarily the result of concentration quenching and crossover relaxation, which can be suppressed by keeping the Ce^{3+} dopant concentration far below 0.7 mol%, whereas for temperatures above 600 K thermal ionization is the predominating quenching process. This new insight into the interplay between different thermal quenching processes provides design principles for optimizing the light emittance and colour stability of new phosphor materials used in white lighting devices characterized by certain operating temperatures.

Received 11th August 2020,
Accepted 23rd September 2020

DOI: 10.1039/d0tc03821k

rsc.li/materials-c

1 Introduction

Inorganic phosphors are of considerable interest for application in phosphor converted white light emitting diodes (pc-WLEDs)[1–3] and over the last decades a large number of compounds have been synthesized.[4] Among the most widely used phosphors is yttrium aluminium garnet ($Y_3Al_5O_{12}$, YAG), which when substituted with a few percent of the activator ion Ce^{3+} to replace Y^{3+} ($Y_{3-z}Ce_zAl_5O_{12}$, YAG:x%Ce^{3+}) gives rise to yellow-green light emission in the 500–700 nm range, based on electronic 5d–4f transitions, upon excitation with a blue light source.[4,5] This material is the prototype of the luminescent materials for pc-WLEDs. Its energy efficiency, however, is limited by a phenomenon known as thermal quenching, which takes place inside the phosphor and leads to a pronounced reduction of the emission intensity of the phosphor at elevated temperatures, typically a few hundred degrees centigrade, as well as alters the white balance (colour) of pc-WLED devices. For YAG:Ce^{3+} with a Ce^{3+} concentration of 3.33 mol%, for example, the emission intensity at 520 K has dropped to about half of that at 300 K.[6] However, the degree of thermal quenching is also shown to vary significantly for different Ce^{3+} concentrations and excitation wavelengths.[6]

Although the response of luminescence efficiency upon temperature change for YAG:Ce^{3+} is well established for different Ce^{3+} concentrations and excitation wavelengths, a consensus regarding the underlying mechanisms has not been reached.[7,8] Generally, thermal quenching in Ce^{3+}-doped phosphors exhibiting electronic 4f–5d transitions is thought to result from one or several of three processes: (1) thermal ionization of the Ce^{3+} 5d electron into the conduction band (CB) of the YAG host crystal followed by charge trapping at defects acting as luminescence killer centres [Fig. 1(a)],[7,9] (2) thermally activated nonradiative energy migration among Ce^{3+} ions to luminescence killer centers (known as concentration quenching) [Fig. 1(b)],[10–12] and (3) thermally activated 5d → 4f crossover relaxation *via* electron–phonon coupling [Fig. 1(c)].[9,13–15]

[a] *Department of Chemistry and Chemical Engineering, Chalmers University of Technology, SE-412 96 Göteborg, Sweden. E-mail: maths.karlsson@chalmers.se; Tel: +46 317726770*

[b] *Luminescent Materials Laboratory, Department of Biotechnology, University of Verona and INSTM, UdR Verona, Strada Le Grazie 15, I-37134 Verona, Italy*

[c] *Radboud University, Institute for Molecules and Materials, FELIX Laboratory, Nijmegen, The Netherlands*

[d] *Nanomaterials Research Group, Department of Biotechnology, University of Verona and INSTM, UdR Verona, Strada Le Grazie 15, I-37134 Verona, Italy*

† Electronic supplementary information (ESI) available. See DOI: 10.1039/d0tc03821k

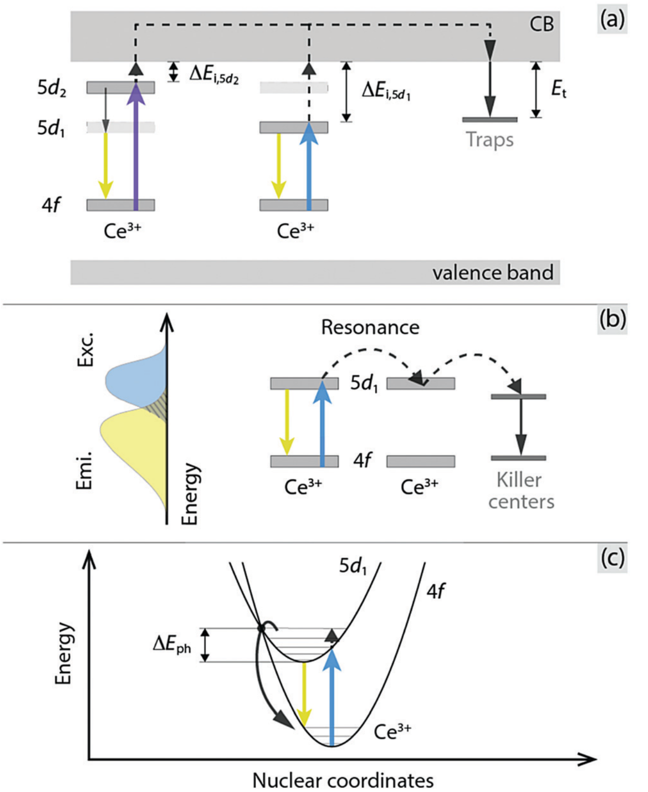

Fig. 1 Schematic illustration of (a) thermal ionization of the Ce^{3+} electron in the $5d_1$ or $5d_2$ excited state into the CB of the host crystal followed by charge trapping at defect levels, (b) thermally activated concentration quenching by nonradiative energy migration among Ce^{3+} ions to killer centers (the overlap between the excitation (Exc.) and emission (Emi.) spectra is indicated to the left, and the extent of overlap determines the probability of resonance transfer of excitation energy between Ce^{3+} ions), and (c) thermally activated crossover from the $5d_1$ excited state to the 4f ground state *via* electron–phonon coupling. $5d_1$ denotes the lowest-energy-laying level of the 5d configuration of Ce^{3+}. The figure is modified from ref. 16 (Copyright 2018 American Chemical Society).

The first type of process (thermal ionization) is predominantly dependent on the energy difference between the emitting level of the Ce^{3+} ion and the CB minimum, which is here called ionization energy. Recent bandgap engineering studies on YAG:Ce^{3+} and cation-substituted variants, combined with studies of vacuum referred binding energy (VRBE) diagrams and thermoluminescence (TL) excitation experiments, show that the quenching is stronger when the ionization energy is smaller.[17–21] The second type of process (nonradiative energy migration among Ce^{3+} ions to luminescence killer centers) is usually argued on the basis of an observed decrease of the (onset) quenching temperature with increasing Ce^{3+} concentration. In comparison, the third type of process (5d → 4f crossover relaxation), which relates to nonradiative relaxation due to coupling between the excited state electrons of Ce^{3+} ions and lattice vibrational modes, is primarily based on theoretical and empirical predictions.[9,22]

With regard to the general effect of temperature increase on the spectroscopic properties of YAG:Ce^{3+}, there is an increasing overlap between the excitation and emission spectra of YAG:Ce^{3+}, especially for high Ce^{3+} concentrations, that leads to increased energy migration among Ce^{3+} ions and thus to an increased probability of trapping the migrating excitation energy by defects.[11] Bachmann *et al.*[6] attributed, in a systematic investigation of YAG:Ce^{3+} with 0.033, 0.33, 1.0, and 3.33 mol% Ce^{3+} doping, the lower quenching temperature for 1.0, and 3.33 mol% Ce^{3+} to an effect of thermally activated concentration quenching. However, the possibility of Ce^{3+} concentration dependent crossover relaxation (as the incorporation of Ce^{3+} may soften the crystal structure and hence increase the phonon population at a given temperature)[16,23] and/or thermal ionization (as the incorporation of Ce^{3+} may cause changes of the ionization energy) should not be neglected in the elucidation of a full understanding of the thermal quenching behaviour of YAG:Ce^{3+} and other materials alike. In particular, because of the many experimental challenges of probing explicitly energy migration and electron–phonon coupling processes in materials, it is only through the combinatorial use of experimental and theoretical techniques, including novel machine learning methods to screen thermally robust phosphors,[24] that a mechanistic understanding of thermal quenching is likely to emerge.

Here we present a systematic analysis of the thermal quenching of luminescence in YAG:x%Ce^{3+}, as a function of Ce^{3+} concentration (x = 0.2, 1, 2, and 3) and temperature (T = 80–860 K), based on a multitechnique approach. The techniques used are photoluminescence (PL), TL, and mode-selective vibrational excitation (together with thermal simulations) techniques. Our results show that the thermal quenching is caused by the combined effect of thermal ionization, thermally activated concentration quenching, and thermally activated 5d → 4f crossover relaxation *via* electron–phonon coupling, with different weights depending on the temperature. This new insight into the interplay between different thermal quenching processes provides design principles for optimizing the light emittance and colour stability of new phosphor materials used in white lighting devices characterized by certain operating temperatures, *e.g.* >150 °C under high-power operating conditions.[25]

2 Results and discussion

2.1 Photoluminescence decay time and quantum yield

Fig. 2(a) shows the temperature dependence of the luminescence decay time, τ, for YAG:Ce^{3+} with a Ce^{3+} concentration corresponding to 0.2, 1, 2, and 3 mol%. All decay curves can be adequately described by a single-barrier quenching model (solid lines) according to

$$\tau(T) = \frac{1}{\Gamma_r + \Gamma_n \exp(-\Delta E/k_B T)}, \quad (1)$$

where Γ_r is the radiative rate, Γ_n is the attempt rate of nonradiative processes, k_B is the Boltzmann constant, and ΔE is the activation energy for the overall quenching behaviour. ΔE is found to decrease from 1.11 eV for the lowest Ce^{3+} dopant concentration to 0.32 eV for the highest one [Table 1 and Fig. 2(b)]. The thermal quenching temperature, $T_{50\%}$, which is defined here as the temperature at which the luminescence efficiency (estimated from decay time or quantum yield data)

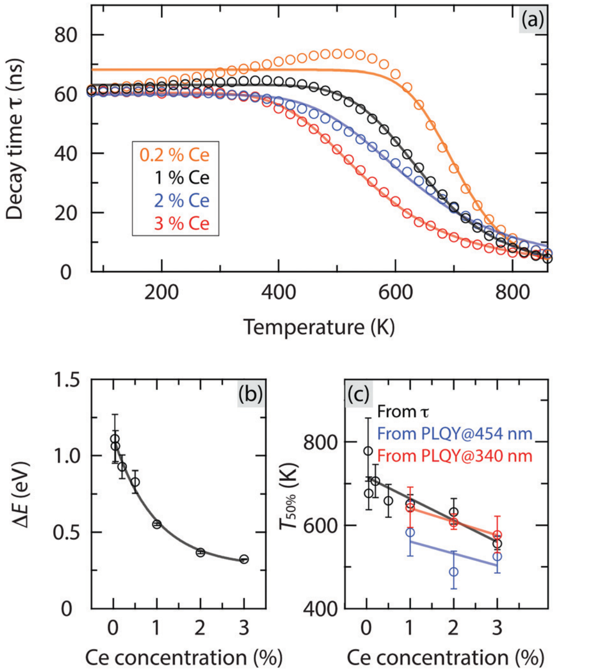

Fig. 2 (a) Temperature dependence of τ for YAG:x%Ce^{3+} with x = 0.2, 1, 2 and 3 for excitation at 454 nm; see Fig. S1 (ESI†) for luminescence decay curves. The solid lines are fits to a single-barrier quenching model. (b) Ce^{3+} concentration dependence of ΔE obtained from eqn (1). (c) Ce^{3+} concentration dependence of $T_{50\%}$. The black line shows $T_{50\%}$ as extracted from the temperature dependence of τ in (a). The blue and red lines show $T_{50\%}$, as extracted from the temperature dependence of the PLQY data, as measured for excitation at 454 nm and 340 nm (see Fig. 3), respectively.

becomes 50% of the low-temperature value, decreases from 778 K for 0.033 mol% to 556 K for 3 mol% [Table 1 and Fig. 2(c)].

Fig. 3 shows the temperature dependence of the internal PL quantum yield (PLQY) for YAG:Ce^{3+} with a Ce^{3+} concentration of 1, 2, and 3 mol%, upon excitation at 454 nm and 340 nm, respectively. The PLQY is only weakly affected by temperature increase up to about 300–500 K. For higher temperatures, the PLQY decreases drastically with increasing temperature, in a way quite similar to the luminescence decay time [Fig. 2(a)]. For excitation at 454 nm, the $T_{50\%}$ values are generally lower by 30–140 K compared to the $T_{50\%}$ values as extracted from the luminescence decay time (Table 1). This discrepancy is most likely associated to multiple light scattering events, which take place in the integrating sphere during the PLQY measurements and which enhance the probability for re-absorption of the emitted light and thereby thermal quenching at a specific temperature. Given this fact, we treat the PLQY data in a qualitative rather than quantitative manner. The validity of a qualitative analysis is further supported by the very similar Ce^{3+} concentration dependence of $T_{50\%}$ derived from the PLQY and luminescence decay time data, respectively [Table 1 and Fig. 2(c)]. In order to unravel the underlying mechanisms of these observations, we determine the activation energy for each type of thermal quenching process for YAG:Ce^{3+}. This is done on the basis of a combined analysis of different optical experiments and the VRBE diagram and is described in the following section.

2.2 Optical spectra and VRBE diagram analysis

Fig. 4(a) shows the diffuse reflectance/transmittance spectra of YAG:x%Ce^{3+} with x = 0.2, 1, 2, and 3 mol%, as measured at room temperature (RT). The two dips in the spectra at around 340 and 460 nm correspond to the 4f → $5d_2$ and 4f → $5d_1$ (absorption) transitions of Ce^{3+}, which are denoted by λ_{5d_2} and λ_{5d_1}, respectively (Table 1). The magnitude of these dips increases generally with increasing Ce^{3+} concentration, as expected from the Beer–Lambert law.[28] The corresponding emission spectra [Fig. 4(b and c)] were measured for excitation at 340 and 454 nm, respectively, and show one asymmetric broad band between approximately 500 and 700 nm. The emission spectra are almost identical for excitation at 340 nm and 454 nm, suggesting that the electronic-vibrational crossing from the $5d_2$ (higher) to $5d_1$ (lower) orbital excited states of Ce^{3+} is a very fast process, followed by a change of (local) structural dynamics arising from vibrational relaxation. Therefore, this change of structural dynamics around the luminescent Ce^{3+} ions has no significant effect on the subsequent $5d_1$ → 4f emission process of Ce^{3+}. It follows that the emission characteristics of the Ce^{3+} 4f–5d transitions are very similar regardless of different excitation energies. However, the significant difference in the energy positions between the $5d_1$ and $5d_2$ levels with respect to the CB minimum of the YAG host should be manifested by significantly different thermal ionization energies of the Ce^{3+} 5d electrons in these two levels.

Using the respective energies of the 4f → $5d_2$ and 4f → $5d_1$ absorption transitions of Ce^{3+} (associated with λ_{5d_2} and λ_{5d_1}, respectively), and the energy positions of the bottom of the CB (E_c) and the 4f level of Ce^{3+} (E_{4f}), we constructed the VRBE diagram of Ce^{3+} in YAG, see Table 1. This analysis shows that the thermal ionization energy for the $5d_1$ level ($\Delta E_{i,5d_1}$) is about 5–8 times larger than that for the $5d_2$ level ($\Delta E_{i,5d_2}$), see Fig. 1(a) and Table 1. Both $\Delta E_{i,5d_1}$ and $\Delta E_{i,5d_2}$ increase slightly with increasing Ce^{3+} concentration, as an effect of a lowering of the $5d_1$ and $5d_2$ levels (red-shifting effect). This shows that the thermal ionization process is very weakly dependent on the Ce^{3+} concentration for $\leq$3 mol% Ce^{3+}.

$\Delta E_{i,5d_1}$ takes on values in the range of 1.11–1.13 eV for variable Ce^{3+} concentration. For the lowest Ce^{3+} concentrations (0.033 and 0.05 mol%), *i.e.* when the Ce^{3+} concentration is so low so that the Ce^{3+} ions in all likelihood can be considered as isolated luminescent centers,[6] $\Delta E_{i,5d_1}$ is quite similar to ΔE (1.06–1.11 eV, see Table 1). In effect, this suggests that for these Ce^{3+} concentrations, thermal quenching is mainly, if not fully, governed by thermal ionization. For higher Ce^{3+} concentrations (0.2–3 mol%), $\Delta E_{i,5d_1}$ deviates significantly from ΔE. This deviation increases systematically with increasing Ce^{3+} concentration and points toward that another or other quenching processes, which have activation energies lower than ΔE, increasingly dominate the overall thermal quenching of luminescence.

Further support for the contribution of more than one quenching process to the observed thermal quenching behaviour

Table 1 Compilation of thermal quenching data for YAG:Ce^{3+}: VRBE parameters (E_c: bottom of conduction band, E_{4f}: 4f level of Ce^{3+}, and $\Delta E_{i,5d_1}/\Delta E_{i,5d_2}$: energy difference between E_c and the $5d_1/5d_2$ level of Ce^{3+}), PL spectral data ($\lambda_{5d_1}/\lambda_{5d_2}/\lambda_{emi}$: maximum of the $5d_1/5d_2$/emission band of Ce^{3+}), thermal quenching measures (ΔE, ΔE_{TL} and ΔE_{ph}: activation energies obtained from decay time, TL, and FELIX experiments, respectively, $T_{50\%}$: thermal quenching temperature, and η_{loss}: loss of luminescence efficiency with respect to the one at 80 K), and PLQY, for YAG:Ce^{3+} with varying Ce^{3+} concentration and average distance between Ce^{3+} ions (R_{Ce})

YAG:Ce^{3+}	Ce^{3+} concentration (mol%)						
(R_{Ce}) (Å)	0.033[a] (36.5)	0.05[b] (31.7)	0.2 (20.0)	0.5[c] (14.8)	1 (11.8)	2 (9.5)	3 (8.3)
VRBE parameters & spectral data (exc. 340/454 nm)							
E_c[d] (eV)				−1.71			
E_{4f}[d] (eV)				−5.52			
λ_{5d_1} (nm)	—	—	459	—	459	459	462
$\Delta E_{i,5d_1}$[e] (eV)	—	—	1.11	—	1.11	1.11	1.13
λ_{5d_2} (nm)	—	—	340	—	342	343	345
$\Delta E_{i,5d_2}$[e] (eV)	—	—	0.16	—	0.18	0.20	0.22
λ_{emi} (nm)	—	—	540	—	541	543	552
Decay time							
ΔE	1.11	1.06	0.93	0.83	0.55	0.37	0.32
$T_{50\%}$ (K)	778	677	706	659	652	632	556
η_{loss}[f] (%)	1	9	6	19	30	41	62
PLQY (exc. 454 nm)							
PLQY[g] (%)	—	—	—	—	79	85	84
$T_{50\%}$ (K)	—	—	—	—	583	488	525
η_{loss}[f] (%)	—	—	—	—	54	71	74
PLQY (exc. 340 nm)							
PLQY[g] (%)	—	—	—	—	51	42	61
$T_{50\%}$ (K)	—	—	—	—	642	607	577
TL (exc. 450 nm)							
ΔE_{TL} (eV)	—	—	—	0.5	0.29[h]	0.25[h]	0.15[h]
FELIX (exc. 454 nm)							
ΔE_{ph} (eV)	—	—	—	—	—	—	0.23

[a] Reproduced from ref. 6. [b] Reproduced from ref. 26 [c] Reproduced from ref. 20. [d] Cited from ref. 19 and 27. [e] Derived by assuming that the E_c and E_{4f} values are independent of Ce^{3+} concentration (for the studied range). [f] Estimated at 600 K. [g] Measured at 300 K. [h] Derived from the TL glow curves corresponding to *trap*3.

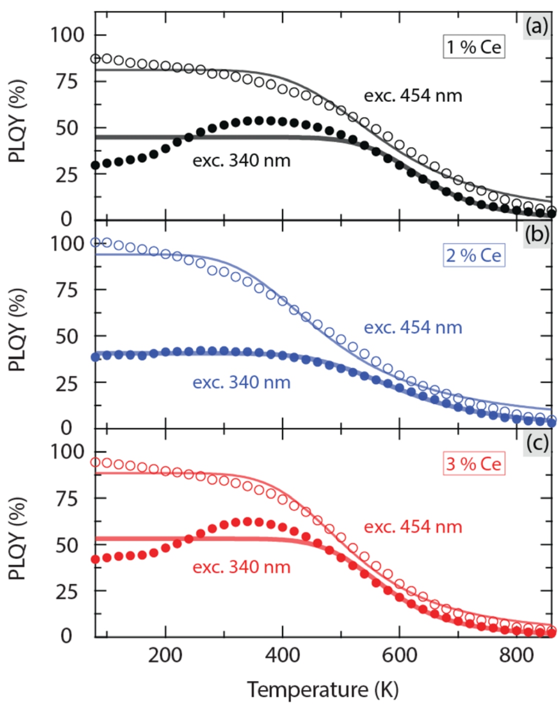

Fig. 3 Variable temperature PLQY of YAG:x%Ce^{3+} with x = (a) 1, (b) 2 and (c) 3 for excitation at 454 nm and 340 nm, respectively; see Fig. S2 (ESI†) for luminescence spectra with respect to the one of the excitation source.

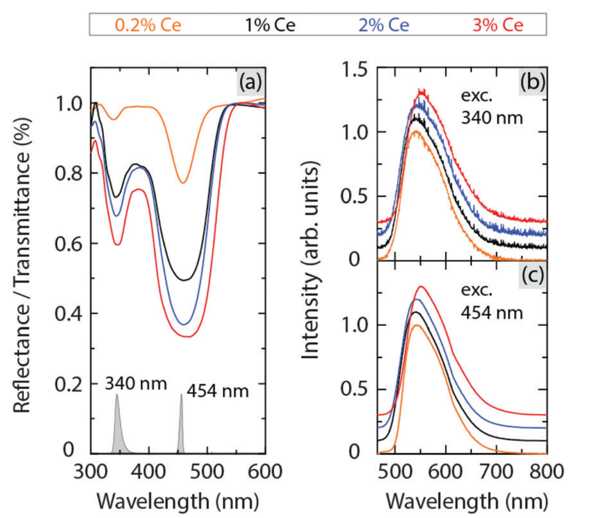

Fig. 4 (a) Diffuse reflectance/transmittance spectra of YAG:x%Ce^{3+} (x = 0.2, 1, 2 and 3). The spectra have been vertically offset and smoothed (see Fig. S3, ESI† for the raw spectra). (b and c) Emission spectra of YAG:x%Ce^{3+} (x = 0.2, 1, 2 and 3) for excitation at 340 and 454 nm, respectively. The spectra of the respective excitation sources, normalized to the band maxima, are shown by the grey areas in (a).

of YAG:Ce^{3+} comes from the analysis of the temperature dependence of PLQY data as measured upon varying excitation wavelengths (340 nm and 454 nm, see Fig. 3). Interestingly, the thermal stability of the PLQY (estimated from $T_{50\%}$) for excitation at 340 nm is higher than that at 454 nm, *cf.* Fig. 2(c). Since the photon irradiation at 340 nm corresponds to excitation to the $5d_2$ level, which is closer to the CB minimum than the $5d_1$ level, this should cause stronger thermal ionization at a given, sufficiently high, temperature and should be reflected in a lower thermal stability of PLQY. In effect, the reverse behaviour as observed here suggests that thermal ionization is not the predominating quenching process for these higher Ce^{3+} concentrations (1–3 mol%). Rather, the systematic decrease of $T_{50\%}$ with increasing Ce^{3+} concentration [Fig. 2(c)] suggests that either thermally activated energy transfer processes to luminescence killer centers, or/and Ce^{3+} concentration induced nonradiative 5d → 4f crossover-relaxation processes are at play.

2.3 Optical spectra and Ce–Ce distance analysis

As far as energy transfer processes between different Ce^{3+} ions are concerned, their probability is thought to depend on the overlap between the absorption and emission bands and the distances between Ce^{3+} ions, see Fig. 5(a and b). In the case of $YAG{:}Ce^{3+}$, the spectral overlap is as high as about 5% of the absorption/emission spectrum at RT [Fig. 5(c)]. It implies that 5% of excited energy has a certain probability of being energetically transferred to other Ce^{3+} ions in $YAG{:}Ce^{3+}$.

Physically, energy transfer may occur as a consequence of electric dipole–dipole interactions of Ce^{3+} ions with a rate P_{Ce}. The critical distance R_c, for such energy transfer processes is defined as the distance between Ce^{3+} ions for which P_{Ce} is equal to the radiative rate of Ce^{3+}. R_c can be estimated using the following equation,[10–12]

$$R_c^6 = (6.3 \times 10^{27}) Q_{abs} \int \frac{F_{abs}(E) f_{emi}(E)}{E^4} dE. \quad (2)$$

Here, Q_{abs} is the absorption strength of Ce^{3+} and takes on a value of 5.55×10^{-19} cm^2 eV, as we have derived from the integrated absorption cross section of Ce^{3+} (see Fig. S4, ESI†). $F_{abs}(E)$ and $f_{emi}(E)$ are the absorption and emission spectral bands that are normalized to unity, respectively, and E is the photon energy.

Using the spectral data in Fig. 5(a), we obtain R_c = 13 Å. This value is in agreement with the one reported by Blasse[12] on the basis of the same model [eqn (2)]. This implies that when the Ce^{3+} concentration is higher than 0.7 mol% [Fig. 5(d)], the effect of energy-transfer induced concentration quenching is comparable with radiative transitions of Ce^{3+}. In addition, the energy transfer rate is found to increase upon elevating temperature due to the twin effect of an increased spectral overlap and a red-shift of the luminescence spectra,[30] see Fig. S5 (ESI†). Therefore, we infer that in order to suppress thermally activated concentration quenching, the Ce^{3+} concentration should be far lower than 0.7 mol%. A lowering of the Ce^{3+} concentration can be also believed to reduce the amount of Ce^{3+} induced defects such as anion vacancies and local structural distortions,[7,23,31] which may act as luminescence killer centers, *cf.* Fig. 1(b), in a manner of, *e.g.*, charge trapping.

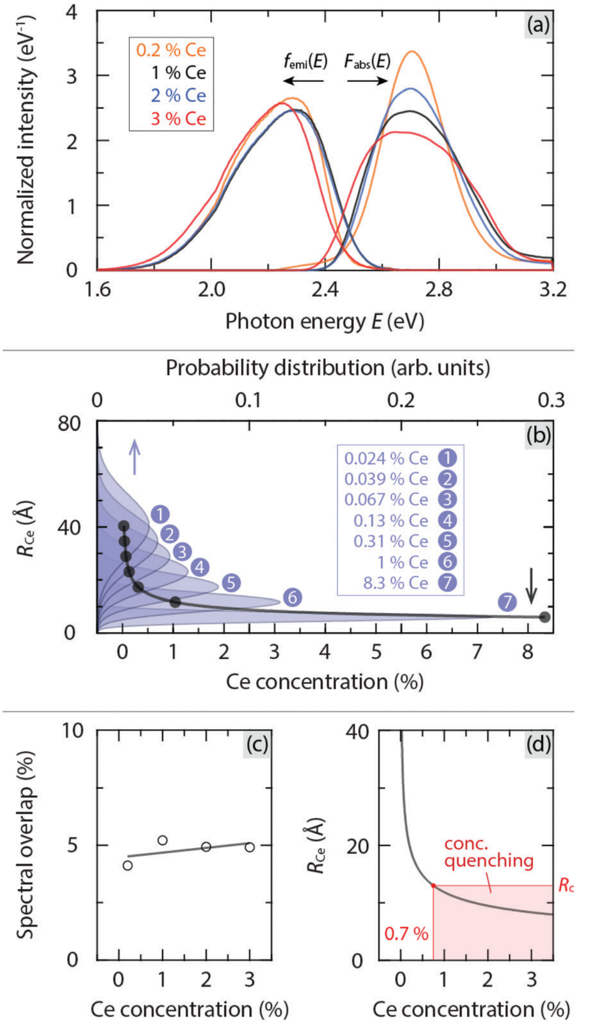

Fig. 5 (a) Normalized absorption and emission spectra of $YAG{:}x\%Ce^{3+}$ (x = 0.2, 1, 2 and 3) at RT, denoted as $F_{abs}(E)$ and $f_{emi}(E)$, respectively, which were derived from the data in Fig. 4. Note that the Kubelka–Munk function $(1 - R)^2/2R$, where R is the reflectance, was used to covert diffuse reflectance to absorption spectra.[29] (b) Average distance between Ce^{3+} ions (R_{Ce}) as a function of Ce^{3+} concentration, as determined from the probability distribution of R_{Ce} for a given Ce^{3+} concentration, see the Methods section for details. (c) Spectral overlap for $YAG{:}x\%Ce^{3+}$ as a function of Ce^{3+} concentration. (d) A close-up of (b) in relation with the critical distance R_c, highlighting the lower limit of the Ce^{3+} concentration for concentration quenching to occur.

Information about the defect structure and charge-trapping dynamics in $YAG{:}Ce^{3+}$ can be obtained from TL experiments.

2.4 Thermoluminescence glow curve measurements

Fig. 6 shows the TL glow curves for $YAG{:}1–3\%Ce^{3+}$, as a function of excitation temperature T_{ex} between 280 K and 700 K. For each material, we observe three distinct glow curve bands when T_{ex} = 280 K and their positions and intensity change significantly upon varying T_{ex}, see Fig. 6 top and bottom, respectively. When the intensity of the glow curve bands reaches their maxima at variable T_{ex}, the positions of the bands are determined, which are for example centred at

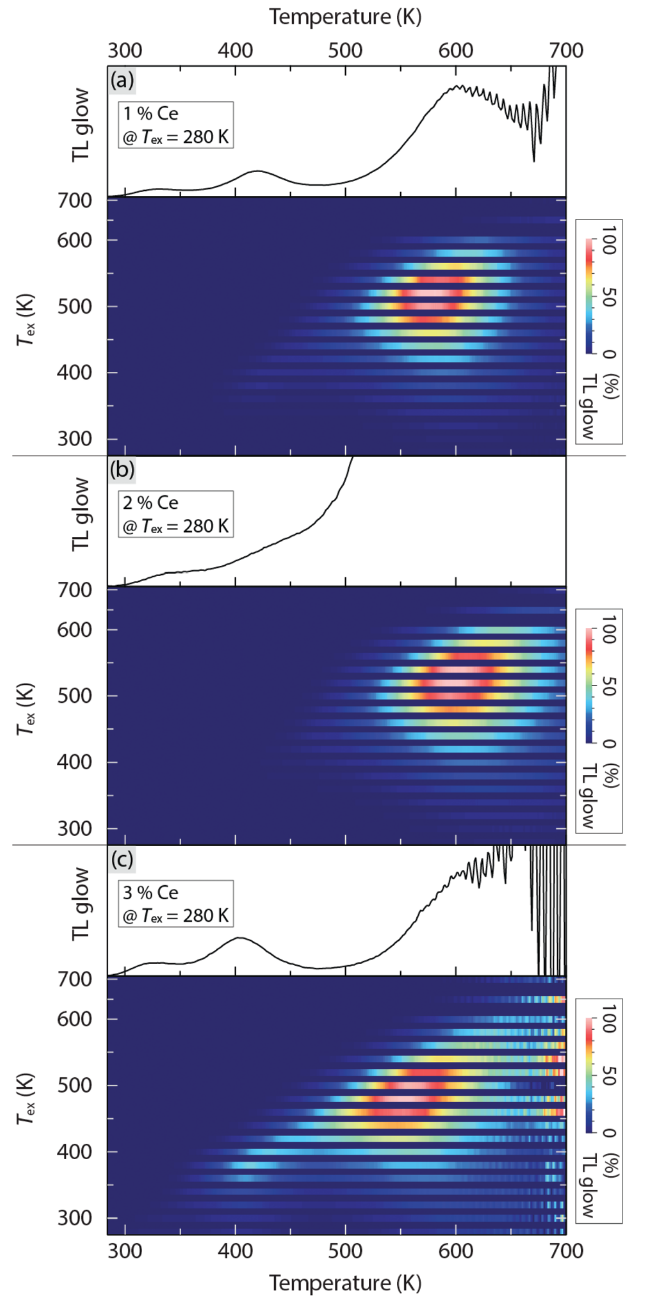

Fig. 6 TL glow curves of YAG:x%Ce^{3+} with (a) x = 1, (b) x = 2, and (c) x = 3, plotted as a function of increasing temperature from 280 K to 700 K with [bottom in (a–c)] T_{ex} varying from 280 K to 700 K and [top in (a–c)] for T_{ex} = 280 K.

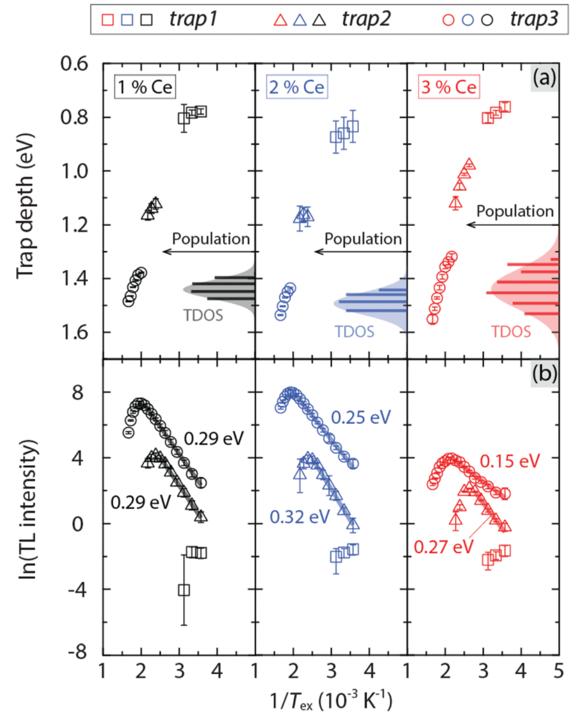

Fig. 7 (a) Trap depth below the CB minimum and TDOS (fitted with a Gaussian distribution), and (b) integrated intensity of TL glow curve bands, for the three traps in YAG:x%Ce^{3+} (x = 1, 2 and 3), plotted as a function of $1/T_{ex}$.

approximately T_m = 325, 415, and 560 K for 3% Ce^{3+}, respectively, where T_m is referred to as the temperature corresponding to the maximum of a glow curve band. The glow curve bands correspond to different types of charge-trapping defects, here labelled as *trap1*, *trap2*, and *trap3*, respectively. On the basis of the T_m values and first-order TL kinetics, we determine the energy difference between the respective trap and CB (here called the trap depth E_t) according to

$$\beta E_t/k_B T_m{}^2 = s\exp(-E_t/k_B T_m), \qquad (3)$$

where β is the heating rate (2 K s^{-1}), s is a frequency factor ($1\times\ 10^{11}$ s^{-1} for YAG:Ce^{3+}),[20] and k_B is the Boltzmann constant. For example, for 3% Ce^{3+}, E_t takes on values of 0.76 eV (*trap1*), 0.98 eV (*trap2*) and 1.33 eV (*trap3*), respectively, *cf.* Fig. 7(a).

The activation energy for charge filling the respective trap, ΔE_{TL}, can be extracted from the T_{ex} dependence of the integrated intensity of the TL glow curve bands, where T_{ex} should be below the temperature at which the trap is filled to each maximum. This analysis points toward a strict Arrhenius dependence with ΔE_{TL} taking on values between 0.15 and 0.32 eV [Fig. 7(b)]. Since all ΔE_{TL} values are significantly smaller than the activation energy for thermal ionization of the Ce^{3+} $5d_1$ electron into the CB ($\Delta E_{i,5d_1}$ ≈ 1.1 eV, see Table 1), this indicates a higher probability of direct charge migration/trapping from the Ce^{3+} ions to defect states, in comparison with charge trapping through thermal ionization.

Interestingly, the energy position of *trap3* (1.3–1.6 eV below the CB) is lower than the Ce^{3+} $5d_1$ level (1.1 eV below the CB), which implies that the process of de-trapping charges at *trap3* and returning to the $5d_1$ level is energetically unfavourable due to the relatively large energy barrier of 0.2–0.5 eV. Moreover, we observe that for *trap3*, which exhibits the strongest TL intensity among the three traps and, hence, the analysis leads to the most reliable results, ΔE_{TL} decreases systematically with increasing Ce^{3+} concentration. In effect, this means that for the higher Ce^{3+} concentrations, the process of trapping the migrating charges of Ce^{3+} at *trap3* becomes more thermally active at a given temperature, which is very likely attributed to enhanced energy transfer among Ce^{3+} ions. In this scenario, we use ΔE_{TL} obtained from *trap3* as the activation energy for thermally activated concentration quenching.

The number of charges in each trap has been also determined from the difference of the TL intensity between two adjacent T_{ex}, where T_{ex} is higher than the temperature resulting in the strongest TL intensity, *i.e.* when T_{ex} is sufficiently high to begin to empty the trapped charges from the trap states.[32,33] From the combined analyses of E_t and the number of trapped charges associated to *trap3*, the trap density of states (TDOS), representing the number of states (population) with respect to E_t, has been determined [Fig. 7(a)]. The TDOS of the deepest trap, *trap3*, can be approximated with a Gaussian distribution for each sample. The bandwidth of the TDOS distribution of *trap3* generally increases upon increasing Ce^{3+} concentration from 1 to 3 mol%. For the shallower traps, *trap2* and *trap1*, the TDOS distribution cannot be determined because of the limited amount of data making the fitting analysis unreliable.

In comparison with the shallower defects that are often associated with non-vacancy defects such as antisite defects,[34–36] the origin of the deepest trap *trap3* is most probably related to oxygen vacancies,[31,37] which are known to act as electron traps and are energetically favourable to be formed in a reducing environment,[37,38] as in the case of our sample preparation. This statement is further supported by the vanished TL glow in YAG:Ce^{3+} after high-temperature annealing in air.[31] We thus infer that the broadening of the TDOS distribution for *trap3* upon increasing Ce^{3+} concentration may be caused by increased local structural disorder and distortions nearby the Ce^{3+} ions.[16,23] This local structural effect changes the coordination environments of the O vacancies and thus leads to a larger variation of the energy levels of the traps related to these vacancies. This effect becomes more pronounced as the Ce^{3+} ions replace the smaller Y^{3+} ions in the neighbourhood of O vacancies.[31] As a result, this TDOS broadening effect may enhance the interactions between Ce^{3+} ions and trap states and further increase the probability for charges to be trapped, which leads to the effect of lowering ΔE_{TL}. We infer that the combined observations of a systematically increasing energy transfer rate (Fig. 5) and a broadening of the TDOS (Fig. 7), with a simultaneously decreasing $T_{50\%}$ [Fig. 2(c)] as a function of increasing Ce^{3+} concentration, confirms the contribution from concentration quenching to the overall quenching behaviour of YAG:Ce^{3+}. However, we also notice the decreasing Debye temperature Θ_D upon increasing the Ce^{3+} concentration from 0 to 3 mol%, which reflects a general softening of the YAG lattice.[23] As Θ_D is a key measure for thermal stability/downconversion efficiency of luminescence,[24,39,40] the apparent correlation between Θ_D and $T_{50\%}$ implies the involvement of nonradiative 5d → 4f crossover relaxation in YAG:Ce^{3+}. We investigated this process using mode-selective vibrational excitation techniques.

2.5 Mode-selective vibrational excitation experiments

Fig. 8 summarizes the results from the two-laser experiment combining a pulsed tunable infrared (IR) laser from FELIX with a pulsed 454 nm blue laser. The aim of this experiment is to investigate the effect of coherent large-amplitude excitation of IR active vibrational modes (phonons) on the luminescence decay time, τ, and thus to get information about possible electron–phonon coupling mechanisms associated with non-radiative crossover relaxation processes. Fig. 8(a) shows τ as a function of the wavenumber of the IR irradiation over the range $\approx$460–900 cm^{-1} for YAG:3%Ce^{3+}. The lower part of the figure shows the IR spectrum of YAG:3%Ce^{3+}, as well as the total energy of an IR macro-pulse; Fig. S7 (ESI†) shows a scheme of the experimental setup. As can be observed, τ is overall shortened, from a few nanoseconds up to several nanoseconds as a function of increasing temperature from 300 K to 450 K, especially in the high wavenumber region (650–900 cm^{-1}) where the IR irradiation is relatively strong. The solid lines in Fig. 8(a) are the simulated τ estimated by considering (only) the heating effect of the IR pre-pulse excitation, as discussed in the Methods section. The simulated τ mimics quite well the energy profile of the IR macro-pulse, with a relatively weak effect in the regions of low IR absorbance, *e.g.* 600–650 cm^{-1} and 850–900 cm^{-1}.

Fig. 8(b) shows the experimentally determined τ subtracted by the simulated τ, here denoted as $\Delta\tau$, which is the response of the mode-selective excitation of IR active phonons on τ. Clearly, the selective excitation of the three highest-frequency phonons at 698, 724, and 789 cm^{-1}, which are assigned to different asymmetric bending motions of the local CeO_8 dodecahedra,[16] depopulates the light-emitting levels of Ce^{3+} in a nonradiative way. Moreover, the magnitude of $\Delta\tau$ increases progressively with increasing temperature of the sample.

To further investigate this temperature dependence, we take the average of $\Delta\tau$, here denoted as $\Delta\tau_{ave}$, over the wavenumber range 650–860 cm^{-1}. $\Delta\tau_{ave}$ follows an Arrhenius dependence with a characteristic activation energy ΔE_{ph} = 0.23 eV, see Fig. 8(c) and Table 1. *A priori*, ΔE_{ph} could relate to either one or a combination of the three possible thermal quenching processes (Fig. 1). However, because ΔE_{ph} is far lower than $\Delta E_{i,5d1}$, vibrationally stimulated ionization of Ce^{3+} ions seems unlikely. In contrast, ΔE_{ph} is closer to ΔE_{TL}, suggesting that ΔE_{ph} relates to vibrationally stimulated concentration quenching. In addition, it is also possible to relate to vibrationally stimulated 5d → 4f crossover *via* electron–phonon interactions in the material. Based on the $5d_1$ → 4f crossover model, ΔE_{ph} thus corresponds to the energy barrier for thermal quenching activated by mode-selective vibrational excitation, see Fig. 1(c).

One may note that, whereas the activation of vibrational modes for 5d → 4f crossover relaxation is obvious, concentration quenching should as well be promoted by the increased probability of energy resonance between Ce^{3+} ions with the help of vibrational excitation. Further, we note that the heating of the sample, due to the increase of applied temperature, has the effect of activating the modes in the low wavenumber region (<300 cm^{-1}), which primarily relate to localized motions of Ce^{3+} ions.[16] This suggests that the vibrationally induced thermal quenching may need the excitation of multiple types of phonons.

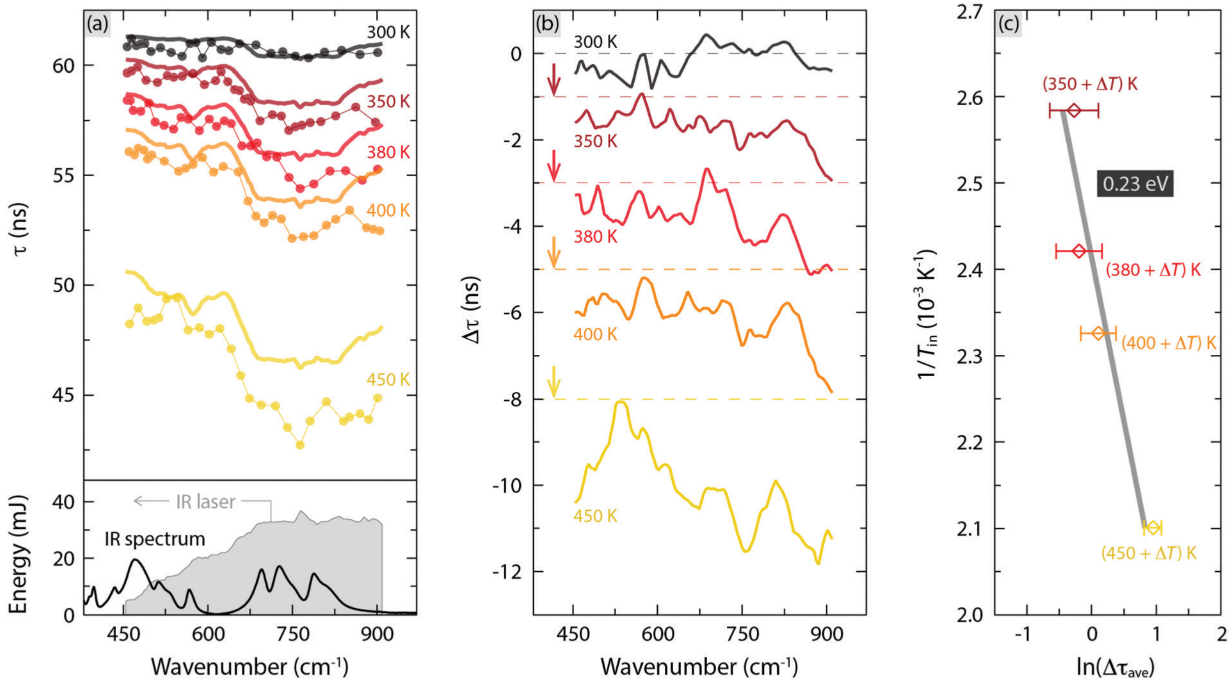

Fig. 8 (a) Top: Experimental decay time τ (dots) of YAG:3%Ce^{3+} for excitation at 454 nm and variable wavenumber of the IR photons, together with the simulated τ (thick line) of the same sample. The measurements were performed at (applied) temperatures of 300 K, 350 K, 380 K, 400 K, and 450 K. Bottom: IR absorbance spectrum of YAG:3%Ce^{3+}, which is reproduced from ref. 16. (Copyright 2018 American Chemical Society), and total energy of the IR irradiation (grey shaded area) as a function of wavenumber. (b) Difference between the experimental and simulated decay times ($\Delta\tau$), which is offset by 1 ns, 3 ns, 5 ns and 8 ns for the data at 350 K, 380 K, 400 K, and 450 K, respectively. (c) *In situ* temperature (T_{in}) dependence of $\Delta\tau_{ave}$ (the average of $\Delta\tau$ over the range of 650–860 cm^{-1}), where T_{in} = applied temperature + the temperature increment due to the IR heating effect (ΔT), see Fig. S6 (ESI†), showing an Arrhenius dependence with an activation energy ΔE_{ph} of 0.23 eV.

2.6 Overall picture of the thermal quenching mechanisms

To sum up the results so far, the three quenching processes appear to be all involved in thermal quenching of luminescence, at least for YAG:3%Ce^{3+} since the magnitude of ΔE (= 0.32 eV) is between $\Delta E_{i,5d1}$ (= 1.13 eV) and ΔE_{TL} (= 0.15 eV) or ΔE_{ph} (= 0.23 eV). Under the assumptions that the radiative rate Γ_r is temperature independent[9,41] and that the nonradiative rates of the three quenching processes increase exponentially with temperature, eqn (1) can be modified as follows,[41]

$$\tau(T) = 1/[\Gamma_r + \Gamma_{n1}\exp(-E_{n1}/k_BT) + \Gamma_{n2}\exp(-E_{n2}/k_BT)]. \quad (4)$$

Here, Γ_{n1} is the nonradiative rate for thermal ionization, and Γ_{n2} reflects a combined nonradiative rate for concentration quenching and 5d → 4f crossover. Note that the latter two processes are here treated as one, because their activation energies are too close to each other to be distinguished. Therefore, E_{n1} equals $\Delta E_{i,5d1}$ and E_{n2} equals the average of ΔE_{TL} and ΔE_{ph}. A free fit of eqn (4) to $\tau(T)$ of YAG:3%Ce^{3+} [Fig. 2(a)] yields Γ_r (= 1.61×10^7 s^{-1}), Γ_{n1} (= 4.24×10^{15} s^{-1}) and Γ_{n2} (= 7.72×10^8 s^{-1}). Using these results, we have calculated the temperature dependence of the ratios of the radiative/nonradiative transition rates to the total transition rate. The result shows that the temperature dependence of the calculated ratio for the radiative transition is in good agreement with that of the experimental $\tau(T)$ (Fig. 9). Most importantly, we observe that the combined effect of concentration quenching and 5d → 4f crossover quenching contributes predominantly to the thermal quenching up to about 600 K, whereas at higher temperatures it

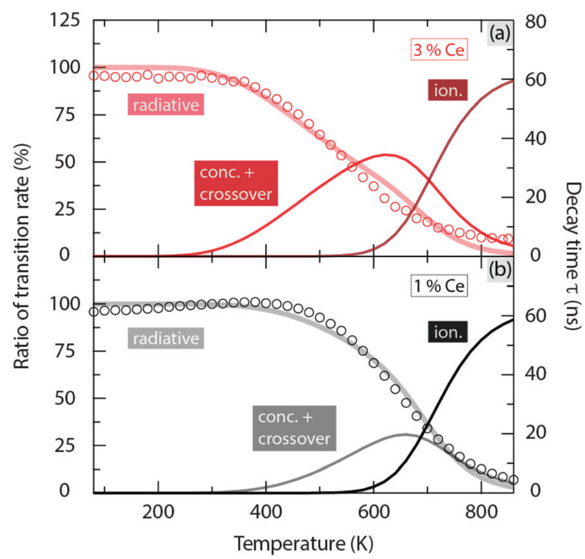

Fig. 9 Left axis: Ratios of the radiative and nonradiative (thermal ionization and combined concentration and 5d → 4f crossover quenching) transition rates of YAG:x%Ce^{3+} with respect to the total transition rate, plotted by solid curves. Right axis: Luminescence decay time of YAG:x%Ce^{3+} (x = 1 and 3), plotted by circles. (a) x = 3 and (b) x = 1.

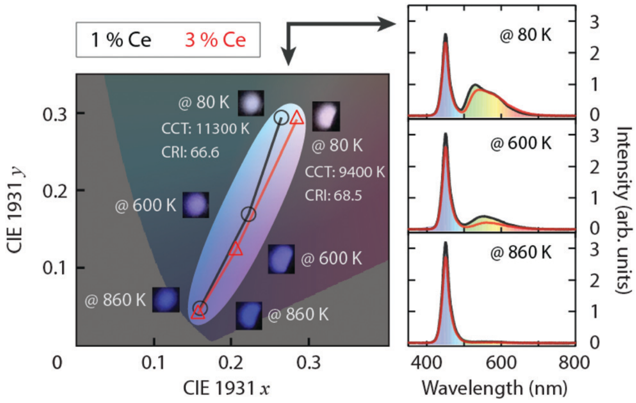

Fig. 10 Left: CIE 1931 coordinates of artificial white light (inset) generated from a 450 nm blue LED and YAG:x%Ce^{3+} (x = 1 and 3) at the temperatures 80 K, 600 K, and 860 K, converted from the emission spectra to the right.

is dictated by thermal ionization. Interestingly, a similar result is obtained for YAG:1%Ce^{3+} [Fig. 9(b)] using the same method under the assumption that ΔE_{ph} is the same for 1 and 3 mol% Ce^{3+} dopant concentrations. However, it is noticed that the most significant and important difference between the two samples is the contribution from combined concentration and crossover quenching, which clearly shows that lowering the Ce^{3+} concentration improves greatly the thermal resistance against thermal quenching especially when the operating temperature is below 600 K, see Fig. 9.

2.7 Generation and evaluation of artificial white light

Emission spectra of artificial white light generated from a blue LED and YAG:Ce^{3+} with 1 and 3 mol% Ce^{3+} show an evident decrease in intensity in the green-yellow region (500–600 nm) upon elevating temperature from 80 K to 860 K (Fig. 10 right). This leads to an effect of shifting the emission colour from bluish white towards pure blue, as shown by their CIE 1931 coordinates in Fig. 10 left. Especially, upon increasing the temperature from 80 K to 600 K, this colour shifting effect is found to be much stronger for the higher Ce^{3+} concentration (3 mol%) even though the white balance of its emission at 80 K is characterized by warmer and more natural white light as indicated by the lower correlated color temperature (CCT) and higher color rendering index (CRI), see Fig. 10 left. This phenomenon can be explained by the fact that the loss of the luminescence efficiency at 600 K (η_{loss}) for YAG:3%Ce^{3+} (η_{loss} = 74%) is more pronounced than that for YAG:1%Ce^{3+} (η_{loss} = 54%), see Table 1, which is mainly the result of enhanced concentration and crossover quenching, as discussed above.

3 Summary and conclusions

We have shown that thermal quenching of luminescence in Ce^{3+}-doped YAG is caused by a combined effect of thermal ionization, thermally activated concentration quenching, and thermally activated 5d → 4f crossover relaxation *via* electron–phonon coupling, and establish the general trends upon variation of the Ce^{3+} concentration and temperature. For temperatures below 600 K, thermal quenching in YAG:Ce^{3+} is primarily the result of concentration quenching and 5d → 4f crossover relaxation. Concentration quenching can be suppressed by keeping the Ce^{3+} dopant concentration far below 0.7 mol%, which reduces considerably the probability for energy transfer between Ce^{3+} ions and, eventually, nonradiative relaxation at luminescence killer centers in a manner of charge trapping, most probably associated with O vacancies of the YAG host lattice. A general strategy of enhancing the structural rigidity by decreasing the Ce^{3+} concentration shows the potential to improve the resistance against thermal quenching of luminescence, since fewer phonon modes are activated. In particular, the activation of high-frequency phonons, which are mainly associated with asymmetric bending motions of the local CeO_8 moieties, shows the effect of inducing nonradiative relaxation through most probably 5d → 4f crossover processes. For temperatures higher than 600 K, the thermal quenching is instead primarily dictated by thermal ionization, which can be suppressed by increasing the ionization energy *via* different cation co-substitution strategies. For lighting device applications, it is found that the energy efficiency of YAG:Ce^{3+} can be saved by 20% at an operating temperature of 600 K by reducing the Ce^{3+} concentration from 3 to 1 mol%. A scenario thus emerges in which the development of new strategies of optimizing the light emitting efficiency and colour stability of new phosphor materials by control over the thermal quenching routes, which depend ultimately on the operating temperature, through the tuning of dopant concentration and ionization energy.

4 Methods

4.1 Sample preparation

Powder samples of $Y_{3-z}Ce_zAl_5O_{12}$ with z = 0.03, 0.06, and 0.09 (corresponding to YAG:x%Ce^{3+} with x = 1, 2, and 3) were prepared by solid state synthesis. These are the very same samples as characterized and investigated in preceding studies focusing on structural and vibrational analyses.[16,23] The epitaxial 50 μm single-crystal film of YAG:0.2%Ce^{3+} was purchased from CRYTUR Ltd in the Czech Republic.

4.2 Diffuse reflectance and transmittance spectroscopy measurements

Diffuse reflectance spectra of the YAG:Ce^{3+} powder samples were measured using a halogen lamp (HLX 64655, Elfa Distrelec AB) as excitation source, and an integrating sphere (IS200-4, Thorlabs) and an UV-VIS spectrometer (USB2000+, Ocean Optics) for the detection of the reflected light. The spectrum of a powder sample of SiO_2, acquired using the same experimental setup, was used as reference. Measurements were performed for temperatures between 80 K and 860 K, and the temperature was controlled using a heating stage from Linkam (THMS 600). For YAG:Ce^{3+} thin film sample, the spectrum was measured in transmittance mode at RT using the same setup, but the sample was placed in a different configuration.

4.3 Photoluminescence measurements

PL emission spectra of the YAG:Ce^{3+} powder samples were measured for temperatures between 80 K and 860 K, using the same setup as used for the diffuse reflectance spectroscopy measurements (see above) but with different excitation sources. For excitation in the blue region, a pulsed laser (DeltaDiode-450L, HORIBA Scientific), with a peak wavelength at 454 nm and a repetition rate of 100 MHz and a pulse width of 80 ps, was used. For excitation in the UV region, we used a continuous-wave UV LED (M340D3, Thorlabs) with a nominal wavelength of 340 nm, powered by 5 V. Note that the emission spectra of YAG:0.2%Ce^{3+} were measured using an optical fiber probe close to the sample instead of using the integrating sphere that led to very weak emission intensity. For PL decay curve measurements, also at temperatures between 80 K and 860 K, we used the pulsed 454 nm laser (DeltaDiode-450L, HORIBA Scientific), but with the repetition rate adjusted to 500 kHz. For the detection of the emitted light, we used a photosensor (H10721-20, Hamamatsu) coupled to a 500 nm longpass filter (A10033-62, Hamamatsu). The temperature was controlled by a Linkam THMS 600 stage.

4.4 Ce–Ce distances analysis

Ce–Ce distances in YAG:Ce^{3+} were determined by calculating the probability distribution of the distances between two Ce^{3+} ions that occupy on any two Y sites (with an equal probability of site occupation) in a super cell comprising n^3 YAG unit cells, where $n = 1, 2, 3, \ldots$ and 7 correspond to Ce^{3+} concentrations of 8.3, 1.0, 0.31,... and 0.024 mol%, respectively [Fig. 5(b)] and using crystallographic data of YAG as published in ref. 42. The mean value of the probability distribution of the Ce^{3+} distances is taken as the average distance between Ce^{3+} ions (R_{Ce}) for a corresponding Ce^{3+} concentration. Using the relation between R_{Ce} and Ce^{3+} concentration, which can be well fitted to a power function, we can estimate R_{Ce} for any specific Ce^{3+} concentration in YAG:Ce^{3+}, see Fig. 5(b) and Table 1. Interestingly, the result using this combined structural and mathematical model is very similar to the one derived from the relation $R_{Ce} = [3/(4\pi N)]^{1/3}$, where N is the density of Ce^{3+} in YAG:Ce^{3+}.[43,44] Using the same crystallographic data as above,[42] for which $N = 1.3867 \times 10^{26}$ ions m^{-3} for 1% Ce^{3+} that scales linearly with Ce^{3+} concentration, we obtain R_{Ce} = 37.4, 32.5, 20.5, 15.1, 12.0, 9.5 and 8.3 Å for 0.033, 0.05, 0.2, 0.5, 1, 2 and 3 mol% Ce^{3+} doping, respectively (see Table 1 for comparison).

4.5 Thermoluminescence glow curve measurements

For the TL measurements, the excitation of charge storage was achieved by photon irradiation at different excitation temperatures (T_{ex} = 280–700 K), using a continuous-wave blue LED at 450 nm for 2 min, which was immediately followed by fast cooling (100 K min^{-1}) to 280 K. After a thermal equilibration time of 1 min (at 280 K), TL glow curves were measured by detecting the emitted light as a function of increasing temperature from 280 K to 700 K with a heating rate of 2 K s^{-1}. The TL signal was monitored using a photosensor (H10721-20, Hamamatsu) and an oscilloscope (DSO-X 2022A, Agilent Technologies). TL glow curves unbiased of the effect of thermal quenching of luminescence were determined by taking the ratio of the measured TL signal and the temperature dependent luminescence intensity.[20] The samples, in the form of powders, were held in crucibles of aluminum and their temperature was controlled using a Linkam THMS 600 heating stage.

4.6 Mode-selective vibrational excitation measurements

The mode-selective vibrational excitation experiments were performed at the free electron laser facility FELIX at Radboud University, The Netherlands.[45] FELIX generates a pulsed, monochromatic beam of photons, which is tuneable in a wide IR range, *e.g.* between 100 cm^{-1} and 3600 cm^{-1}, thus making it possible to excite selectively IR active lattice vibrational modes (phonons) of YAG:Ce^{3+}.[16] For this purpose, the wavelength of the IR light was scanned over the range 11–22 μm ($\approx$460–900 cm^{-1}) with a step size of 0.1 μm, while detecting *in situ* the PL decay curve of YAG:3%Ce^{3+} using a photosensor (H10721-20, Hamamatsu) and a 500 nm long-pass filter in front upon pulsed excitation at 454 nm (DeltaDiode-450L, HORIBA Scientific), see Fig. S7 (ESI†) for the experimental setup. In this way, features in the PL decay characteristics specifically associated with the excitation of specific IR active phonons were measured. Of importance here, the FELIX light pulses consist of macro-pulses with a pulse width of 5–10 μs and a repetition rate of 10 Hz, and for which each macro-pulse consists of a 1 GHz train of micro-pulses of a few ps duration (Fig. S7, ESI†). The 454 nm excitation was triggered in the middle of each macro-pulse.

The sample was prepared as a disc-shaped pellet containing approximately 20 wt% of YAG:3%Ce^{3+} in 50 mg CsI, and was held in a custom-made heating block. It should be noted that CsI is transparent in the wavenumber range of interest (460–900 cm^{-1}) and hence does not contribute to any peaks in the vibrational spectrum. CsI is also transparent in the visible region and hence does not contribute to any effects related to the 454 nm excitation and the emission of YAG:Ce^{3+}. To suppress the decrease of the intensity of the IR light associated with the absorption of air molecules, the measurements were performed inside a custom-made enclosure with flowing N_2. Measurements were taken at the temperatures 300 K, 350 K, 380 K, 400 K, and 450 K.

4.7 Thermal simulations

In order to determine the effect of mode-selective vibrational excitation on the PL decay curve characteristics of YAG:3%Ce^{3+}, one has to account for any local (pre-)heating effects due to the IR irradiation on the sample. To evaluate such heating effects, we simulated the temperature of YAG:3%Ce^{3+}, by mimicking the experimental conditions. Specifically, we considered the effects of

(i) temperature increase due to the mode-selective vibrational excitation by the irradiation with monochromatic IR light, and

(ii) temperature decrease through spontaneous heat dissipation in the sample, as an effect of any thermal gradient in the system (sample + surrounding).

To determine the spatial and temporal distribution of thermal energy resulting from (i) and (ii), respectively, the bulk of the disc-shaped sample, made of YAG:3%Ce^{3+} and CsI (diluting agent), whose dimensions measured approximately 7 mm ϕ (xy-plane) $\times$ 0.35 mm thickness (z-direction), was simulated by meshed grids of 0.2 mm (x-axis) $\times$ 0.2 mm (y-axis) $\times$ 0.04 mm (z-axis), coordinated at a position (x, y, z) in the sample, and where the thickness of the sample was calculated by assuming that the mixture of YAG:3%Ce^{3+} and CsI was an ideal solid solution. The respective densities (ρ) for YAG:Ce^{3+} and CsI (4.56 and 4.51 mg mm^{-3}, respectively)[46,47] were assumed to be temperature independent, and CsI was assumed to be completely transparent in the IR and visible regions.

For the simulation of the IR irradiation, the IR laser beam was assumed to be irradiating in the vertical direction (*i.e.* in the z-direction) on the sample. The cross section of the intensity of the IR beam (xy-plane) was set to be a 2D Gaussian distribution with a full width at half-maximum (FWHM) of 1 mm (Fig. S7, ESI†) with an intensity that decreases along the z-direction according to the Beer–Lambert law,[28] which was determined by the IR absorbance of YAG:3%Ce^{3+} (Fig. S8, ESI†). An IR macro-pulse was then simulated by ten pulses of 1 μs duration, separated by an infinitesimal time interval. Together with the measured energy of one IR macro-pulse [Fig. 8(a) bottom], a 3D energy distribution of the simulated IR macro-pulse at any specific time (t) in the interval of 0–10 μs inside the sample at any variable position, $E_{IR}(x,y,z,t)$, was calculated.

By using this computational setting, the thermal effect due to mode-selective vibrational excitation (i) was simulated by[48]

$$\frac{\mathrm{d}T}{\mathrm{d}t} = \frac{E_{\mathrm{IR}}(x,y,z,t)}{C(T)m}, \tag{5}$$

where T is the temperature of the sample unit (*i.e.* meshed grid) at (x, y, z), m is the mass of YAG:Ce^{3+} contained in the sample unit and $C(T)$ is the heat capacity of YAG:Ce^{3+}, see Fig. S9 (ESI†).[49] For the thermal effect of the spontaneous heat dissipation in the sample (ii), we instead used the following equation based on the Fourier's law and the law of energy conservation,[48,50]

$$\frac{\mathrm{d}T}{\mathrm{d}t} = \frac{k_{\mathrm{eff}}(T)}{\rho_{\mathrm{eff}}C_{\mathrm{eff}}(T)}\nabla^2 T. \tag{6}$$

Here, $k_{\mathrm{eff}}(T)$, $C_{\mathrm{eff}}(T)$ and ρ_{eff} are the effective thermal conductivity, heat capacity and density of the sample, respectively (Fig. S9, ESI†).[49,51,52] The effective thermal and materials properties were calculated, by weighing the same properties of YAG:Ce^{3+} and CsI based on their masses and considering their average effect on heat conduction, because the diffusion of thermal energy acted on both materials in the sample.

Using as input in the simulations T = 300 K, 350 K, 380 K, 400 K, and 450 K, that matched the experimental conditions, eqn (5) and (6) were solved. In effect, we obtained the evolution of temperature of the sample units throughout one IR macro-pulse, which could be further spatially averaged to represent the *in situ* temperature of the entire sample. Of particular interest, the *in situ* temperature at the time when the sample was excited by the 454 nm blue laser (*i.e.* after about 5 μs of IR irradiation, see Fig. S7, ESI†) was determined and the result was plotted as a function of the IR wavenumber (Fig. S6, ESI†). From this result, the temperature increment ΔT averaged over the range of 650–860 cm^{-1}, where the thermal effect of the mode-selective vibrational excitation was most effective, was calculated and used for the estimation of non-thermal effects of mode-selective vibrational excitation [Fig. 8(c)].

The heating effect due to the IR irradiation (as described above) on the luminescence decay time of YAG:Ce^{3+} was further simulated. In each PL detection, the decay curve was assumed to be the result of an averaging effect of the light emitted from YAG:Ce^{3+} powder particles that were distributed in different parts of the pellet sample, which were characterised by different temperatures, as discussed above. Therefore, these YAG:Ce^{3+} particles corresponded to different τ values that could be extracted from the experimental τ–T relation [Fig. 2(a)]. Furthermore, the contributions from YAG:Ce^{3+} particles situated at different positions needed to be weighed by the absorption of the 454 nm laser, *i.e.* the energy distribution of the 454 nm laser beam inside the sample. This energy distribution was defined as a 2D Gaussian distribution with a FWHM of 2 mm (x-direction) and 0.7 mm (y-direction) (Fig. S7, ESI†), whose intensity decreased along the z-direction based on the Beer–Lambert law. The absorption cross section of the sample at 454 nm was experimentally measured to be 2.95 $\times$ 10^{-20} cm^2. Although this cross section value was relatively small compared to the one obtained from the single crystal film of YAG:0.2%Ce^{3+} (Fig. S4, ESI†), it should reflect better the real sample condition, *e.g.* light scattering events in a powder made sample. To this end, the average of weighed τ values was used to represent the simulated τ varied upon the IR heating effect [Fig. 8(a)].

4.8 Generation and evaluation of artificial white light

Artificial white light was generated by the irradiation with a blue LED (450 nm, output optical power = 1 μW) on YAG:Ce^{3+}, at the temperatures 80 K, 600 K, and 860 K. The emitted white light was detected using an integrating sphere (IS200-4, Thorlabs) connected to an UV-VIS spectrometer (USB2000+, Ocean Optics). The temperature of YAG:Ce^{3+} was set by a Linkam THMS 600 heating stage.

Conflicts of interest

There are no conflicts to declare.

Acknowledgements

This work was financially supported by the Swedish Research Council FORMAS under grant agreement No. 2013-12723, Bertil & Britt Svenssons Stiftelse för Belysningsteknik, and the European Community's Seventh Framework Programme (FP7/2007-2013) under grant agreement No. 312284. We also acknowledge the FELIX laboratory for access to photon beam facilities and thank Dr A. F. G. van der Meer (FELIX laboratory) for on-site technical support.

References

1 S. Pimputkar, J. S. Speck, S. P. DenBaars and S. Nakamura, Prospects for LED Lighting, *Nat. Photonics*, 2009, **3**, 180–182.

2 P. F. Smet, A. B. Parmentier and D. Poelman, Selecting Conversion Phosphors for White Light-Emitting Diodes, *J. Electrochem. Soc.*, 2011, **158**, R37–R54.

3 M. R. Krames, O. B. Shchekin, R. Mueller-Mach, G. O. Mueller, L. Zhou, G. Harbers and M. G. Craford, Status and Future of High-Power Light-Emitting Diodes for Solid-State Lighting, *J. Disp. Technol.*, 2007, **3**, 160–175.

4 Y.-C. Lin, M. Karlsson and M. Bettinelli, Inorganic Phosphor Materials for Lighting, *Top. Curr. Chem.*, 2016, **374**(21), 1–47.

5 X. Qin, X. Liu, W. Huang, M. Bettinelli and X. Liu, Lanthanide-Activated Phosphors Based on 4f–5d Optical Transitions: Theoretical and Experimental Aspects, *Chem. Rev.*, 2017, **117**, 4488–4527.

6 V. Bachmann, C. Ronda and A. Meijerink, Temperature Quenching of Yellow Ce^{3+} Luminescence in YAG:Ce, *Chem. Mater.*, 2009, **21**, 2077–2084.

7 Y.-C. Lin, M. Bettinelli and M. Karlsson, Unraveling the Mechanisms of Thermal Quenching of Luminescence in Ce^{3+}-Doped Garnet Phosphors, *Chem. Mater.*, 2019, **31**, 3851–3862.

8 P. F. Smet and J. J. Joos, White Light-Emitting Diodes: Stabilizing Colour and Intensity, *Nat. Mater.*, 2017, **16**, 500–501.

9 G. Blasse and B. C. Grabmaier, *Luminescent Materials*, Springer Berlin Heidelberg, 1994.

10 D. L. Dexter, A Theory of Sensitized Luminescence in Solids, *J. Chem. Phys.*, 1953, **21**, 836–850.

11 D. L. Dexter and J. H. Schulman, Theory of Concentration Quenching in Inorganic Phosphors, *J. Chem. Phys.*, 1954, **22**, 1063–1070.

12 G. Blasse, Energy Transfer in Oxidic Phosphors, *Phys. Lett. A*, 1968, **28**, 444–445.

13 C. W. Struck and W. H. Fonger, Unified Model of the Temperature Quenching of Narrow-Line and Broad-Band Emissions, *J. Lumin.*, 1975, **10**, 1–30.

14 C. W. Struck and W. H. Fonger, *Understanding Luminescence Spectra and Efficiency Using W_P and Related Functions*, Springer Berlin Heidelberg, 2012.

15 K. C. Bleijenberg and G. Blasse, QMSCC Calculations on Thermal Quenching of Model Phosphor Systems, *J. Solid State Chem.*, 1979, **28**, 303–307.

16 Y.-C. Lin, P. Erhart, M. Bettinelli, N. C. George, S. F. Parker and M. Karlsson, Understanding the Interactions between Vibrational Modes and Excited State Relaxation in $Y_{3-x}Ce_xAl_5O_{12}$: Design Principles for Phosphors Based on 5d-4f Transitions, *Chem. Mater.*, 2018, **30**, 1865–1877.

17 I. D. Venevtsev, V. Khanin, P. A. Rodnyi, H. Wieczorek and C Ronda, Temperature Quenching of Radio- and Photo-luminescence of $Y_3(Ga,Al)_5O_{12}$:Ce^{3+} and $Gd_3(Ga,Al)_5O_{12}$:Ce^{3+} Garnet Ceramics, *IEEE Trans. Nucl. Sci.*, 2018, **65**, 2090–2096.

18 J. Ueda, K. Aishima and S. Tanabe, Temperature and Compositional Dependence of Optical and Optoelectronic Properties in Ce^{3+}-Doped $Y_3Sc_2Al_{3-x}Ga_xO_{12}$ (x = 0, 1, 2, 3), *Opt. Mater.*, 2013, **35**, 1952–1957.

19 P. Dorenbos, Electronic Structure and Optical Properties of the Lanthanide Activated $RE_3(Al_{1-x}Ga_x)_5O_{12}$ (RE = Gd, Y, Lu) Garnet Compounds, *J. Lumin.*, 2013, **134**, 310–318.

20 J. Ueda, P. Dorenbos, A. J. J. Bos, A. Meijerink and S. Tanabe, Insight Into the Thermal Quenching Mechanism for $Y_3Al_5O_{12}$:Ce^{3+} Through Thermoluminescence Excitation Spectroscopy, *J. Phys. Chem. C*, 2015, **119**, 25003–25008.

21 J. Ueda, S. Tanabe and T. Nakanishi, Analysis of Ce^{3+} Luminescence Quenching in Solid Solutions between $Y_3Al_5O_{12}$ and $Y_3Ga_5O_{12}$ by Temperature Dependence of Photoconductivity Measurement, *J. Appl. Phys.*, 2011, **110**, 053102.

22 G. Blasse, Thermal Quenching of Characteristic Fluorescence, *J. Chem. Phys.*, 1969, **51**, 3529–3530.

23 N. C. George, A. J. Pell, G. Dantelle, K. Page, A. Llobet, M. Balasubramanian, G. Pintacuda, B. F. Chmelka and R. Seshadri, Local Environments of Dilute Activator Ions in the Solid-State Lighting Phosphor $Y_{3-x}Ce_xAl_5O_{12}$, *Chem. Mater.*, 2013, **25**, 3979–3995.

24 Y. Zhuo, A. M. Tehrani, A. O. Oliynyk, A. C. Duke and J. Brgoch, Identifying an Afficient, Thermally Robust Inorganic Phosphor Host *via* Machine Learning, *Nat. Commun.*, 2018, **9**, 4377.

25 A. Setlur, Phosphors for LED-Based Solid-State Lighting, *Electrochem. Soc. Interface*, 2009, **16**, 32–36.

26 M. J. Weber, Nonradiative Decay from 5d States of Rare Earths in Crystals, *Solid State Commun.*, 1973, **12**, 741–744.

27 S. K. Sharma, Y.-C. Lin, I. Carrasco, T. Tingberg, M. Bettinelli and M. Karlsson, Weak Thermal Quenching of the Luminescence in the $Ca_3Sc_2Si_3O_{12}$:Ce^{3+} Garnet Phosphor, *J. Mater. Chem. C*, 2018, **6**, 8923–8933.

28 J. Solé; L. Bausa and D. Jaque, *An Introduction to the Optical Spectroscopy of Inorganic Solids*, Wiley, 2005.

29 B. Schrader, *Infrared and Raman Spectroscopy: Methods and Applications*, Wiley, 2008.

30 Y.-C. Lin, P. Erhart and M. Karlsson, Vibrationally Induced Color Shift Tuning of Photoluminescence in Ce^{3+}-Doped Garnet Phosphors, *J. Mater. Chem. C*, 2019, **7**, 12926–12934.

31 C. R. Varney, D. T. Mackay, A. Pratt, S. M. Reda and F. A. Selim, Energy Levels of Exciton Traps in Yttrium Aluminum Garnet Single Crystals, *J. Appl. Phys.*, 2012, **111**, 063505.

32 A. J. J. Bos, Theory of Thermoluminescence, *Radiat. Meas.*, 2007, **41**, S45–S56.

33 K. Van den Eeckhout, A. J. J. Bos, D. Poelman and P. F. Smet, Revealing Trap Depth Distributions in Persistent Phosphors, *Phys. Rev. B: Condens. Matter Mater. Phys.*, 2013, **87**, 045126.

34 A. B. Muñoz-Garca, E. Artacho and L. Seijo, Atomistic and Electronic Structure of Antisite Defects in Yttrium Aluminum Garnet: Density-Functional Study, *Phys. Rev. B: Condens. Matter Mater. Phys.*, 2009, **80**, 014105.

35 M. Nikl, A. Vedda, M. Fasoli, I. Fontana, V. V. Laguta, E. Mihokova, J. Pejchal, J. Rosa and K. Nejezchleb, Shallow Traps and Radiative Recombination Processes in $Lu_3Al_5O_{12}$:Ce

Single Crystal Scintillator, *Phys. Rev. B: Condens. Matter Mater. Phys.*, 2007, **76**, 195121.

36 M. Nikl, E. Mihokova, J. Pejchal, A. Vedda, Y. Zorenko and K. Nejezchleb, The Antisite Lu_{Al} Defect-Related Trap in $Lu_3Al_5O_{12}$:Ce Single Crystal, *Phys. Status Solidi B*, 2005, **242**, R119–R121.

37 J. Ueda, K. Aishima, S. Nishiura and S. Tanabe, Afterglow Luminescence in Ce^{3+}-Doped $Y_3Sc_2Ga_3O_{12}$ Ceramics, *Appl. Phys. Express*, 2011, **4**, 042602.

38 J. Ueda, S. Miyano and S. Tanabe, Formation of Deep Electron Traps by Yb^{3+} Codoping Leads to Super-Long Persistent Luminescence in Ce^{3+}-Doped Yttrium Aluminum Gallium Garnet Phosphors, *ACS Appl. Mater. Interfaces*, 2018, **10**, 20652–20660.

39 J. Brgoch, S. P. DenBaars and R. Seshadri, Proxies from Ab Initio Calculations for Screening Efficient Ce^{3+} Phosphor Hosts, *J. Phys. Chem. C*, 2013, **117**, 17955–17959.

40 K. A. Denault, J. Brgoch, M. W. Gaultois, A. Mikhailovsky, R. Petry, H. Winkler, S. P. DenBaars and R. Seshadri, Consequences of Optimal Bond Valence on Structural Rigidity and Improved Luminescence Properties in $Sr_xBa_{2-x}SiO_4$:Eu^{2+} Orthosilicate Phosphors, *Chem. Mater.*, 2014, **26**, 2275–2282.

41 B. di Bartolo, *Advances in Nonradiative Processes in Solids*, Springer, New York, 1991.

42 A. Nakatsuka, A. Yoshiasa and T. Yamanaka, Cation Distribution and Crystal Chemistry of $Y_3Al_{5-x}Ga_xO_{12}$ ($0 \leq x \leq 5$) Garnet Solid Solutions, *Acta Crystallogr., Sect. B: Struct. Sci.*, 1999, **55**, 266–272.

43 D. Jaque, M. O. Ramirez, L. E. Bausá, J. G. Solé, E. Cavalli, A. Speghini and M. Bettinelli, $Nd^{3+} \rightarrow Yb^{3+}$ Energy Transfer in the $YAl_3(BO_3)_4$ Nonlinear Laser Crystal, *Phys. Rev. B: Condens. Matter Mater. Phys.*, 2003, **68**, 035118.

44 D. F. De Sousa, F. Batalioto, M. J. V. Bell, S. L. Oliveira and L. A. D. O. Nunes, Spectroscopy of Nd^{3+} and Yb^{3+} Codoped Fluoroindogallate Glasses, *J. Appl. Phys.*, 2001, **90**, 3308–3313.

45 D. Oepts, A. F. G. Van der Meer and P. W. Van Amersfoort, The Free-Electron-Laser User Facility FELIX, *Infrared Phys. Technol.*, 1995, **36**, 297–308.

46 W. M. Haynes, *CRC Handbook of Chemistry and Physics*, CRC Press, 2016.

47 M. Moszyński, T. Ludziejewski, D. Wolski, W. Klamra and L. O. Norlin, Properties of the YAG: Ce Scintillator, *Nucl. Instrum. Methods Phys. Res., Sect. A*, 1994, **345**, 461–467.

48 P. S. Senanayake, J.-P. R. Wells, M. F. Reid, R. B. Hughes-Currie, G. Berden, R. J. Reeves and A. Meijerink, Frequency Non-Degenerate Sequential Excitation of the Impurity Trapped Exciton in Strontium Fluoride Crystals Doped with Ytterbium, *J. Appl. Phys.*, 2015, **117**, 133109.

49 R. J. M. Konings, R. R. Van der Laan, A. C. G. Van Genderen and J. C. Van Miltenburg, The Heat Capacity of $Y_3Al_5O_{12}$ from 0 to 900 K, *Thermochim. Acta*, 1998, **313**, 201–206.

50 R. B. Bird; W. E. Stewart and E. N. Lightfoot, *Transport Phenomena*, Wiley, 2007.

51 J. Hostaša, J. Matějíček, B. Nait-Ali, D. S. Smith, W. Pabst and L. Esposito, Thermal Properties of Transparent Yb-Doped YAG Ceramics at Elevated Temperatures, *J. Am. Ceram. Soc.*, 2014, **97**, 2602–2606.

52 D. Gerlich and P. Andersson, Temperature and Pressure Effects on the Thermal Conductivity and Heat Capacity of CsCl, CsBr and CsI, *J. Phys. C: Solid State Phys.*, 1982, **15**, 5211.